Surface Instability of Liquid Propellants in Microgravity During Pulsed Settling Operations

Bryan D. Hoffman[1], Marco D. Sansone[1], and Jacob M. Brodnick[2]

NASA Marshall Space Flight Center, Huntsville, Alabama, USA

Pulsing reaction control system (RCS) thrusters, vent valves, or other propulsion devices can preserve propellant resources in space, but this operation also effectively introduces a vibration to the vehicle. When the vibration is perpendicular to the liquid propellant surface, Faraday waves may be generated at the liquid-vapor interface. These Faraday instabilities can perturb or break up the liquid surface of cryogenic tanks, leading to inefficiencies in thermal management or even ullage collapse. Drawing from theory and experiments, an engineering model defining the allowable design regions for pulsed settling in microgravity was assembled and verified with computational fluid dynamics (CFD) simulations. A traditional settling metric, the Bond number, was also overlaid in the model to indicate which duty cycles were insufficient to overcome surface tension and aggregate propellant. Mission planners and engineers can consult the tool to rapidly evaluate the stability of a liquid-vapor interface given the pulse frequency and the excitation acceleration. Expressions developed for Faraday waves induced by a sinusoidal forcing input at standard gravity were found to provide excellent predictive capabilities for pulsed, or rectangular, waveforms in the absence of a consistent gravitational acceleration. This study extends the usage of these equations to an alternative forcing function and microgravity environments for the purpose of estimating natural frequencies, surface mode shapes, surface wave amplitudes, and the onset of droplet ejection. CFD simulations with the Loci/STREAM-VoF (Volume of Fluid) solver were initially validated against experimental results in standard gravity. Discrete points on the design map were then investigated with CFD and confirmed that the engineering model reliably indicates surface stability and most Faraday wave characteristics without requiring higher-fidelity tools. The engineering model is highly extensible and can be adapted for various propellant fill fractions, fluid properties, and tank sizes.

I. Nomenclature

T	=	pulse, or forcing, period
T_0	=	surface wave period
Bo	=	Bond number
R	=	tank radius
g	=	gravitational acceleration
σ	=	surface tension
ρ	=	liquid density
υ	=	kinematic viscosity
ω	=	pulse, or forcing, angular frequency
ω_0	=	surface wave angular frequency
a_c	=	sinusoidal excitation acceleration at the onset of Faraday waves
k	=	wavenumber

---

[1] Computational Fluid Dynamics Engineer, Jacobs Space Exploration Group, NASA MSFC-ER42
[2] Computational Fluid Dynamics Engineer, NASA MSFC-ER42

1

H	=	liquid surface height from the tank bottom
λ	=	surface wavelength
a_d	=	sinusoidal excitation acceleration at the droplet ejection threshold
b	=	surface wave amplitude

II. Introduction

In microgravity, liquid propellants tend to easily distribute throughout a tank, or unsettle, unless consistent acceleration is applied. This behavior can be problematic for propulsion systems or propellant transfer between tanks due to the risk of vapor ingestion in feed lines or liquid ingestion in vent lines. Unsettling can also submerge ullage gas diffusers, hindering performance of pressurization systems not designed for that mode of operation. Moreover, unsettling can lead to unintentional mixing between a cryogenic liquid and a relatively warm vapor volume above it, known as the ullage. This mixing generates heat and mass transfer between the two phases and can lead to ullage collapse, or the decline of pressure towards saturated conditions.

In architectures without propellant management devices, typical of tanks in large-scale orbital rockets, the acceleration applied to aggregate liquid is commonly produced by reaction control system (RCS) thrusters. These thrusters are allotted a budget of propellant mass for the purpose of settling cryogens. For thrusters with a fixed force output, the amount of propellant mass expended and the average acceleration can be reduced by pulsing, or introducing a time delay between thruster firings. Consequently, a range of average accelerations can be achieved by considering the vehicle mass, the RCS thrust output, the pulse duration, and the duty cycle, or the ratio of the pulse duration to the pulse period. Propulsion engineers are responsible for evaluating these parameters and selecting RCS hardware which satisfy objectives for many mission phases, including for liquid aggregation.

A side effect of pulsing, however, is that a vibration is effectively introduced. Instabilities in liquids within a vibrating container are well known. The polymathic physicist and chemist, Michael Faraday, recorded the first observations in an appendix to his article to the Royal Society of London in 1831 [1]. He documented the observation that liquid on a vibrating plate displayed regular patterns. Notably, he described changes in the behavior of these patterns due to liquid properties, liquid depth, frequency, and force, but not to parameters such as surface size. He even observed the primary ½-subharmonic response of the surface waves. As illustrated in Fig. 1, when the container goes down, the liquid inertia tends to create a surface deformation which disappears when the surface comes back up, completing the excitation period (T). The flow induced from the destruction of the previous waves drives the following waves, whose maxima occur at the location of the prior waves' minima (and vice versa), making the surface wave period (T_0) equal to two excitation periods. At high enough forcing inputs or low enough frequencies, the patterns became chaotic, and splashing occurred. Droplet ejection could be problematic in space applications where ullage collapse is a concern. Unlike experiments done in earth's gravity well, the only significant acceleration propellants experience in space may be from the vehicle's thrusters. At very low frequencies, liquids inclined to wet surfaces may climb the walls between pulses, exaggerating the unsettling effects. Therefore, it is necessary to understand the constraints imposed on RCS thrusters by surface instabilities to adequately design settling operations.
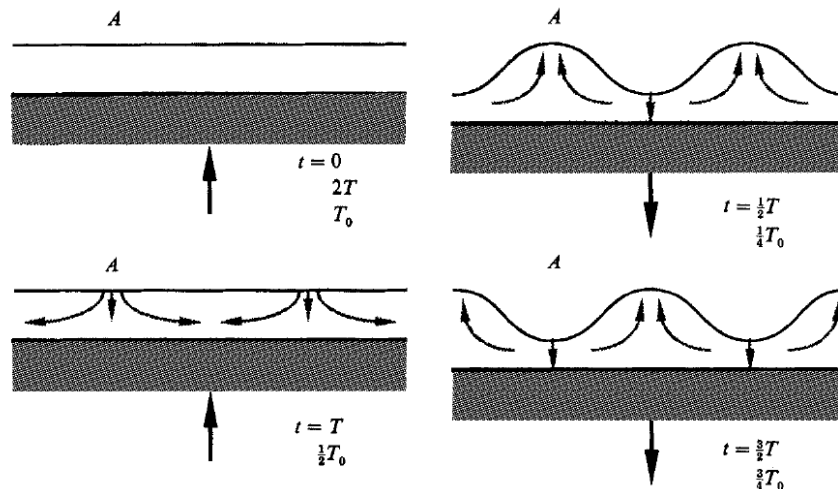
Fig. 1 For an excitation perpendicular to the liquid-vapor interface, the most visible liquid surface response is at half the excitation frequency, known as the ½-subharmonic [2].

III. Engineering Model

A. Theory

The Bond number (Bo) is a well-known metric used to define the relative magnitudes of gravitational acceleration (g) and surface tension (σ) given the tank radius (R), and the liquid density (ρ). By selecting a target Bond number, shown in Eq. (1), the metric provides a constraint on the minimum average acceleration designers must meet to overcome surface tension in microgravity and aggregate liquid reliably. An analysis by Hochstein et al. in 1992 used a 2D computational model with a Volume of Fluid (VoF) approach to evaluate the impact of Bond number on the settling function, a correlation enabling prediction of pulsed settling performance for a wide range of tank sizes [3]. They found that reorientation performance, or the efficiency of the settling operation, is similar for different pulse patterns when the Bond number is greater than 10. As the Bond number was increased from 10 to 100, the model results showed a very narrow range of variation in the settling function, indicating that there was a very strong correlation between average acceleration and the vehicle velocity increment (delta-v), which is proportional to the propellant used to accomplish the maneuver.

$$Bo = gR^2\rho/\sigma \tag{1}$$

When vibrations first begin, an isochronous wave forms at the boundary if there is a meniscus, which is common for cryogenic propellants with low contact angles in microgravity. The size of the meniscus is tied to the capillary length scale, $l_c \approx \sqrt{T/\rho a}$. Since the capillary length is inversely proportional to the root of the instantaneous acceleration (a), ripples are generated due to the shifting capillary length and the conversation of mass, as depicted in Fig. 2. These waves dissipate as they move towards the center of the tank but may interfere with parametric waves, depending on the decay length, $l_d \approx \sigma/(4\nu\rho\omega)$, which is a function of the surface tension, kinematic viscosity (ν), liquid density, and the driving angular frequency (ω). The side wall boundary effects can only be disregarded when the tank radius is significantly greater than the decay length ($R \gg l_d$).
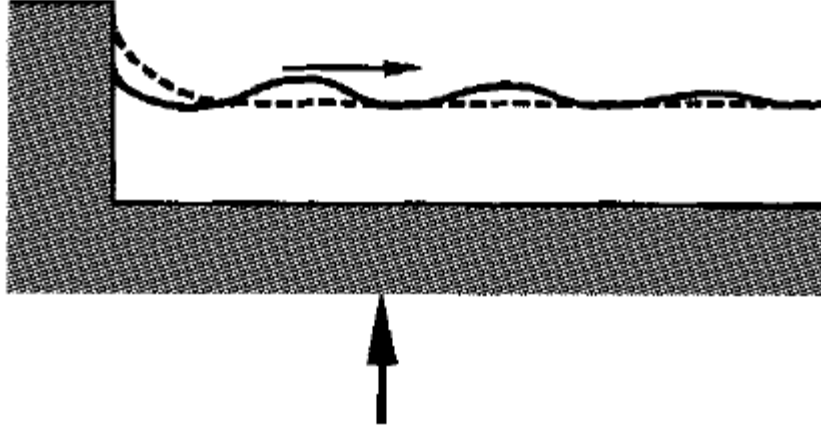
Fig. 2 Meniscus wave propagation from a boundary and its decay [2].

In addition to the Bond number constraint, Faraday instabilities impose limitations on the pulsed settling operating conditions. The onset of parametric waves takes place when the combination of driving frequency and excitation acceleration crosses a stability threshold. A simple estimate of this threshold (a_c) is given in Eq. (2). The equation applies to capillary waves on the surface of low-viscosity liquids with infinite depth [4]. Instability thresholds for ideal fluids were first described theoretically by Benjamin and Ursell by finding the solutions to Mathieu's equation [5]. Later, the theoretical threshold for viscous fluids was expounded by Kumar and Tuckerman by numerically solving the full hydrodynamic system starting from the Navier-Stokes equations [6].

$$a_c = 8(\rho/\sigma)^{1/3}\nu\omega^{5/3} \tag{2}$$

If surface waves are excited, linearized theory using the unsteady Bernoulli equation in Eq. (3) can be used to characterize the response [7]. The principal components are the velocity potential (φ) in Eq. (4), the pressure (p) in Eq. (5), and the interface shape (η) in Eq. (6), assumed to be a sinusoidal wave with amplitude b. The pressure term originates from Eq. (7), which captures the pressure difference across a curved liquid-vapor interface with radii of curvature R_1 and R_2. Solving for the surface wave frequency (ω_0) in the x-z plane produces the dispersion relation in Eq. (8), a relationship between frequency and wavelength. This formula also accounts for the height of the stationary liquid-vapor interface from the tank bottom (H).

$$\frac{\partial \varphi}{\partial t} + \frac{p}{\rho} + g\eta = 0 \tag{3}$$

$$\varphi = \frac{b\omega_0 \cosh\big(k(z+H)\big) \sin(kx - \omega_0 t)}{k \sinh(kH)} \tag{4}$$

$$p_{z=\eta} \cong -\sigma \frac{\partial^2 \eta}{\partial x^2} \tag{5}$$

$$\eta = b\cos(kx - \omega_0 t) \tag{6}$$

$$\Delta p = \sigma\left(\frac{1}{R_1} + \frac{1}{R_2}\right) \tag{7}$$

$$\omega_0{}^2 = \left(k^3 \frac{\sigma}{\rho} + kg\right) \tanh(kH) \tag{8}$$

Faraday waves initially behave very orderly, and this dispersion relation can be used to calculate surface wave frequencies or wavenumbers (k) of the surface response. These orderly waves can be categorized as either gravity or capillary waves. The transition between capillary waves and gravity waves is determined by setting the surface tension term in Eq. (8) equal to the gravitational acceleration term. The result is a crossover wavenumber ($k_{crossover}$), described by Eq. (9). The crossover wavenumber can be reinserted into the dispersion relation to return the gravity-capillary crossover frequency in Eq. (10), which assumes infinite depth ($\tanh(kH) \approx 1$).

$$k_{crossover} = \sqrt{\frac{g\rho}{\sigma}} \tag{9}$$

$$\omega_{0,crossover} = (4g^3 \rho / \sigma)^{1/4} \tag{10}$$

Capillary waves have small wavelengths (λ), and the dominant restoring force is the surface tension. On the other hand, gravity waves are characterized by relatively long wavelengths and weak surface tension. Equation (11) provides the method for converting between wavenumber and wavelength for all propellant tanks and spatial dimensions. Likewise, the radial mode (m) and the circumferential mode (n) can be related to the wavenumber using Eq. (12) and Eq. (13) for rectangular tanks and circular cylinders, respectively. In Eq. (13), ξ is the m-th root of the derivative of the n-th order Bessel function of the first kind. For convenience, the "jnp_zeros" function within the Special submodule of the scipy package in python can be used to compute this term.

$$k = \frac{2\pi}{\lambda} \tag{11}$$

$$k_m = \frac{\pi m}{R} \tag{12}$$

$$k_{nm} = \frac{J'_n(\xi)}{R} \tag{13}$$

Experiments have demonstrated that capillary waves experience predictable droplet ejection independent of the gravitational acceleration. This feature has obvious benefits in low-gravity applications, where the surface tension term would dominate. An example of this behavior is shown in Fig. 3. The sinusoidal excitation acceleration at which droplet ejection occurs (a_d) was empirically determined by Goodridge et al. [8]. Using ethanol, distilled water, and glycerin-water solutions, they recorded the acceleration which produced two ejected droplets within a ten second period. According to their research, the threshold is non-hysteretic for capillary waves, but it does vary by 5-10% for gravity waves, depending on whether it is approached from higher or lower accelerations [9].
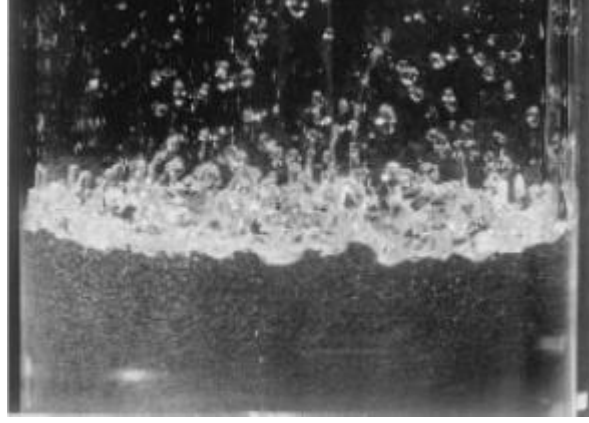
Fig. 3 Droplet-ejecting waves in distilled water at 30 Hz [9].

A theoretical basis for droplet formation comes from the assumption that the ratio of wave amplitude (b) and wavelength approaches unity at the droplet ejection threshold. Mathematically, this ratio (b/λ) was evaluated to be a maximum of 0.73 for capillary waves, exceeding the value of 0.142 for gravity waves [10]. Wave crests become self-intersecting at higher ratios, trapping vapor in the troughs. From observations, the wave amplitude for pure capillary waves can be described by Eq. (14) [8]. Rearranging terms and substituting wavelength for wave amplitude, the excitation acceleration then varies with $\lambda\omega^2$. Taking the gravitational acceleration term as negligible for capillary waves and assuming infinite depth, the dispersion relation from Eq. (8) can be combined with Eq. (11) and $\omega = 2\omega_0$ (subharmonic) to produce Eq. (15). Measured droplet ejection accelerations by Goodridge et al. were fit to this gravity-independent functional form and the coefficient (C_1) determined from a linear regression. Later, the expression was further validated with the addition of an uncertainty range to the coefficient in Eq. (16) [11]. Goodridge notes that the relationship is suitable for low-viscosity fluids and an alternative form was proposed for high viscosity liquids. Note that the droplet ejection equation is independent of tank fill level and tank size; the effects of these factors are primarily observed in the surface response according to Eq. (8).

$$b = 47a/\omega^2 \tag{14}$$

$$a_d = C_1(\sigma/\rho)^{1/3}\omega^{4/3} \tag{15}$$

$$C_1 = 0.26 \pm 0.05 \tag{16}$$

The thresholds for gravity wave breakup are not as well formed. In the other limit, where surface tension is negligible, the droplet ejection acceleration reduces to Eq. (17). Puthenveettil and Hopfinger stated that the coefficient in the gravity wave regime, C_2, is less defined since the relationship between a_d and the wave amplitude at ejection is not unique [11]. They also pointed out that, using a gravity-capillary scaling, the generic relationship in Eq. (18) is produced, where the coefficient (C) and exponent (n) are a function of the driving frequency. In the transition region between pure gravity-dominated breaking ($\omega^* \ll 0.61$) and capillary-dominated breaking ($\omega^* \gg 0.61$), the value of n may be expected to vary from 0 to 4/3. Given the uncertainty in gravity wave ejection threshold, targeting a design to operate in the capillary wave regime is the recommended path to confidently avoid unstable operation.

$$a_d = C_2 g \tag{17}$$

$$\frac{a_d}{g} = a^* = C(\omega/(\omega_{0,crossover}/\sqrt{2}))^n = C\omega^{*n} \tag{18}$$
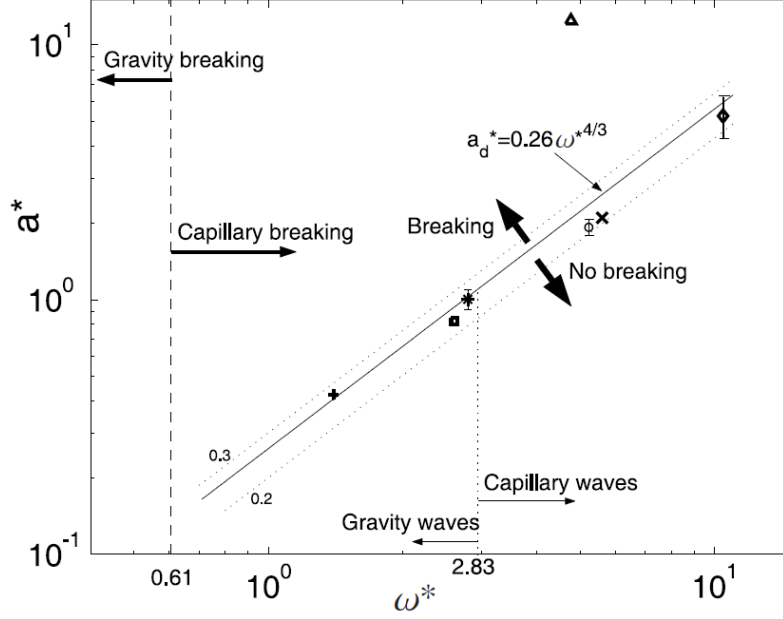
Fig. 4 Droplet ejection threshold vs. forcing frequency, non-dimensionalized by gravity-capillary scaling [11].

B. Pulsed Acceleration Profile

The key parameters in a pulse wave are annotated in the visual overview of Fig. 5. Equation (19) describes a pulsed settling profile where the instantaneous acceleration is a function of the peak pulse acceleration (a_{pulse}), the duty cycle (d), the excitation frequency, and the summation term (n), which is not to be confused with the circumferential mode number from Eq. (13). Equation (20) is the sinusoidal acceleration profile typically assumed by literature and used in the experiments of Goodridge and Puthenveettil. When the amplitude of the sine wave (a_{sine}) induces Faraday waves, its value is a_c. Similarly, when it is high enough to break up the liquid surface, its value is equal to a_d.
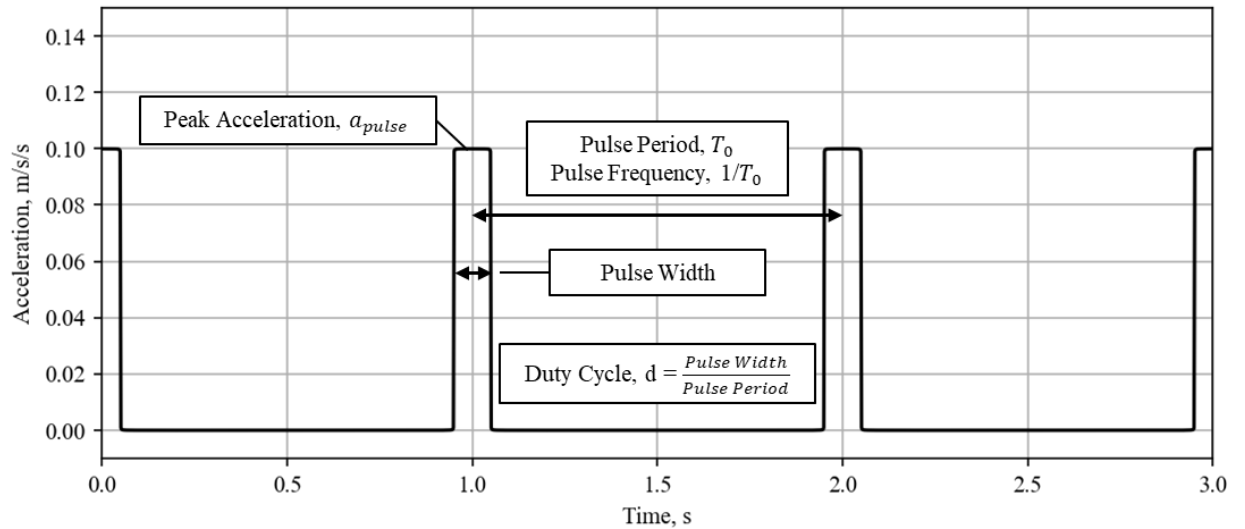

Fig. 5 Description of pulsed, or rectangular, waveform parameters.

$$a = \frac{2a_{pulse}}{\pi} \sum_{n=1}^{\infty} \frac{1}{n} \sin(n\pi d)\cos(n\omega t) + a_{pulse}d \qquad (19)$$

$$a = a_{sine}\cos(\omega t) + g \qquad (20)$$

When $n = 1$, Eq. (19) reduces to the same functional form as Eq. (20). Equating the two produces Eq. (21), which converts the magnitude of a pulse wave into an equivalent excitation amplitude of the sine wave at the same frequency. This conversion from a peak pulse amplitude and duty cycle to an equivalent sinusoidal amplitude is necessary to compare the strength of the excitation against the values of a_c and a_d on a design map. Physically, it represents the contribution of the fundamental frequency to the pulse wave. At low duty cycles, a small angle approximation will simplify the value of a_{sine} to $2a_{pulse}d$, or twice the average acceleration ($g = a_{pulse}d$). Comparisons between a pulse wave and its equivalent sine wave using this method of conversion show good agreement in Fig. 6. Other approaches were considered as well. For example, conserving the area of the pulsed waveform above or below the average. The result was a similar arc as Eq. (21) in the form of $a_{sine} = a_{pulse}\pi(d - d^2)$. However, this produced excitations which were too high, particularly at lower duty cycles.

$$a_{sine} = \frac{2a_{pulse}}{\pi}\sin(\pi d) \qquad (21)$$
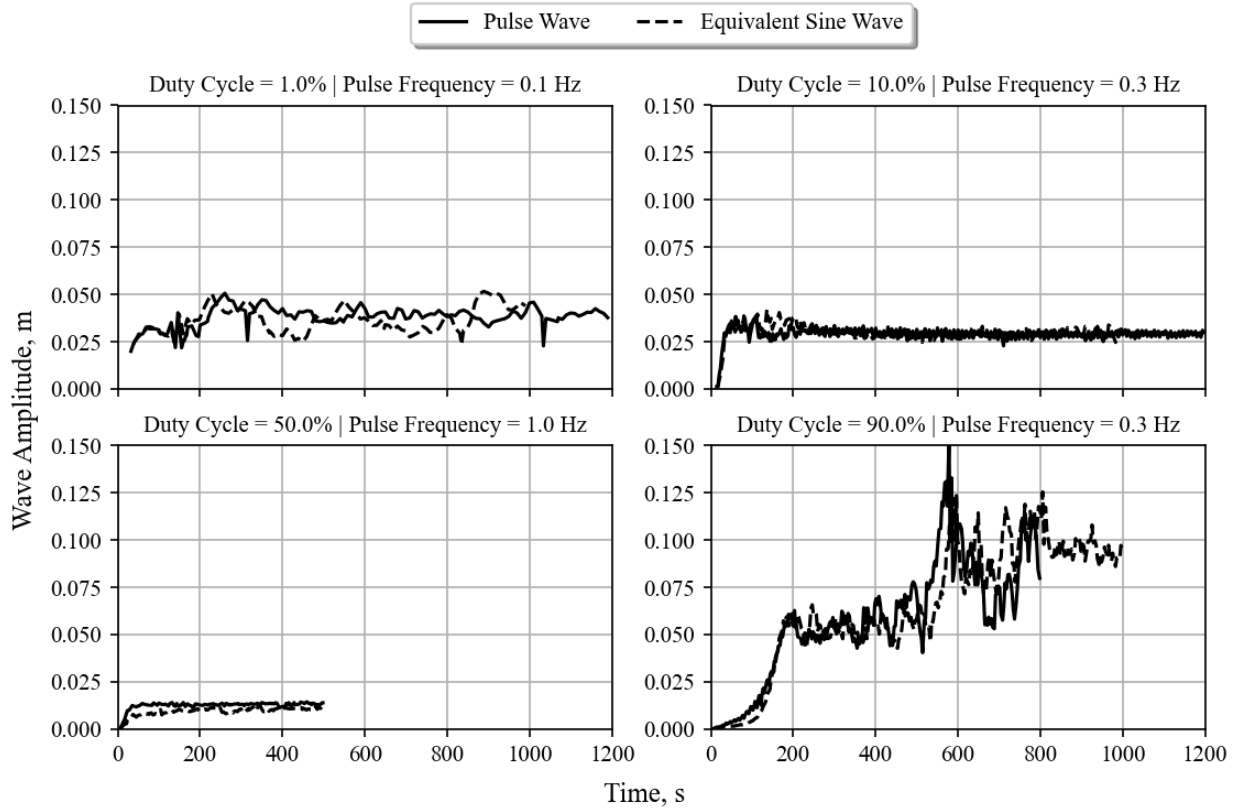
Fig. 6 Wave amplitude vs. time showing the comparison between a pulsed acceleration waveform and an equivalent sine wave using Eq. (21) for various operating conditions in a two-dimensional rectangular tank.

An example of three duty cycles and the magnitude of their associated sinusoidal excitation acceleration is presented in Fig. 7. In the uppermost plots, the pulse frequency and peak acceleration are held constant while the pulse on-time and duty cycle are variable. The lower plot shows the arc of excitation acceleration with duty cycle. In the limits where duty cycle goes to 0% (no on-time) and 100% (no off-time), there is no perturbation to the system.

Thus, the equivalent sine wave amplitude is zero. As the duty cycle is increased from 0%, the excitation amplitude increases until a maximum occurs at 50% duty cycle. Above 50%, the equivalent sine wave amplitude begins to decrease in the same way that it ascended while the average acceleration continues to climb.
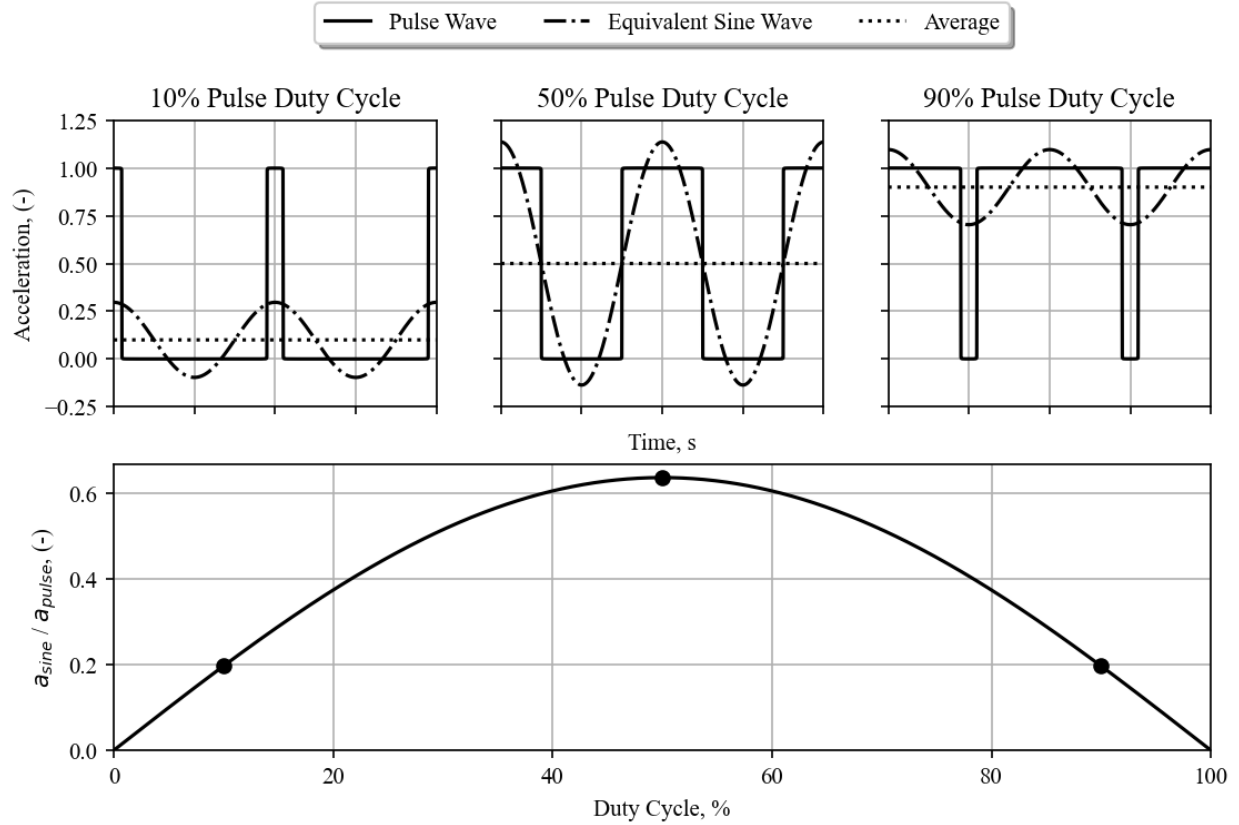
Fig. 7 Examples of pulse waves and their equivalent sine wave amplitudes (10%, 50%, and 90% duty cycles).
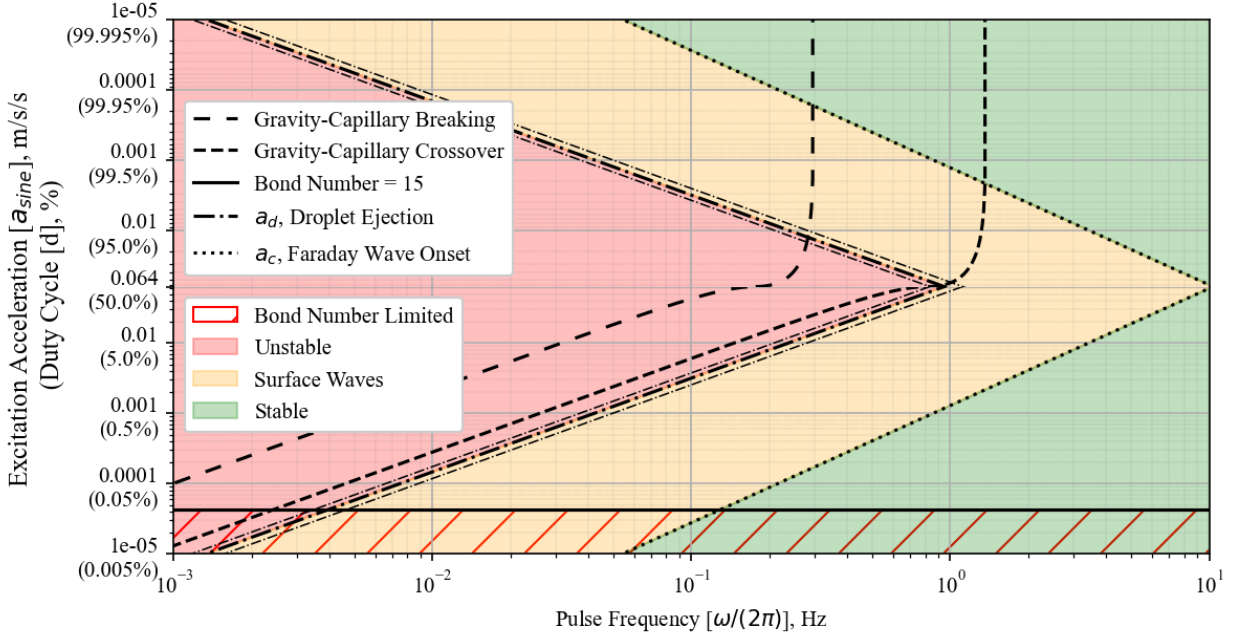
C. Design Map

The practical result of the collection of theory, empirical results, and analytical relationships is the pulsed settling design map in Fig. 8. The map is based on the generic propellant tank and fluid properties presented in section V. With this engineering model, designers can determine whether the operating condition that they have selected is stable, subject to surface waves at the liquid-vapor interface, or unstable by plotting the pulse frequency against the sinusoidal excitation acceleration. For convenience, the duty cycle can be overlaid on the y-axis using the conversion in Eq. (21). The map assumes that a single pulse frequency is maintained and that the operation is performed for a long period of time relative to the pulse period.

Since extreme ranges in duty cycle and frequency are possible, the map is plotted in a log-log scale. Outlined in Fig. 7, the excitation acceleration is a function of the duty cycle and is also symmetric about the 50% value, so the plot is split with the y-axis logarithmically approaching 100% duty cycle at the top and 0% duty cycle at the bottom. It is expected that very low duty cycles are more common than very high ones. This is not only because a common objective of pulsing is to save as much propellant mass as possible, but also because the areas of highest confidence in the equations are where surface tension is much stronger than the average acceleration, falling to the right of the gravity-capillary crossover curve.

The engineering model is divided by color into three regions based on the Faraday wave response. The red, unstable region is characterized by liquid breakup and droplet ejection from the surface, with the boundary determined by Eq. (15). To the right of this boundary – the yellow region – surface waves are predicted to occur at the liquid surface. Wave amplitudes are relatively high near the droplet ejection threshold and decrease to the right, as pulse frequencies increase. The transition from surface waves to a stable, unperturbed surface – the green region – is delineated by the Faraday wave onset formula in Eq. (2).

The gravity-capillary crossover from Eq. (10) is also highlighted, marking the transition from gravity-dominated waves (left) to waves dominated by surface tension (right). Since duty cycle and the average acceleration (effective gravity) are coupled, it runs parallel to the droplet ejection threshold for most of the low duty cycles before deviating around 50%. The deviation occurs because the average acceleration continues to go up with duty cycle while the excitation acceleration trends back down. Note that the droplet ejection threshold is plotted up to 100% even though it lies entirely in the gravity wave regime above 50%. The data points in Fig. 4 indicate there is some applicability of this equation between the gravity-capillary breaking line and the crossover line. This relationship will break down when treading too close to the breaking line, however, since the equation assumes capillary-dominated breaking as discussed in part A ($\omega^* \gg 0.61$).

Fig. 8 Pulsed settling design map for liquid oxygen with a peak pulse acceleration (a_{pulse}) of 0.1 m/s/s, a fill height of 4 m, and a tank radius of 2 m.

A cross-hatched region at the bottom of the map shows the duty cycles at which the Bond number criterion has been violated. While the colored regions inform the user about the stability of an operating condition, the Bond number metric provides an understanding of whether liquid can be brought from an unsettled state to a settled state. If the Bond number is too low, the duty cycle must be increased to overcome surface tension and move the liquid. Ideally, $Bo \gg 1$, and the selection of the Bond number was discussed in the Theory portion of this section. A limit of 15 is plotted because it exceeds the cited literature recommendation of $Bo \geq 10$ and because separate analyses have shown this value to prevent complete wetting at high fill levels. If a range of duty cycles are achievable after consulting the design map, the time it takes to settle the propellant for a single operating condition can be predicted with computational fluid dynamics (CFD). A tradeoff between the total time it takes to aggregate the liquid and the amount of time the propulsive system is operating (e.g., RCS thrusters, propulsive vent system) can then be evaluated for other duty cycles [12]. Designing a settling scheme or selecting hardware to operate in the stable region is not always possible (nor essential, since wave amplitudes may be very low compared with the tank scale). In cases where surface waves are predicted, the wavenumber/mode shape and wave amplitude can be estimated. Verification and discussion of these predictions is addressed in section V.

IV. Droplet Ejection Validation in Standard Gravity

A. Simulation Inputs and Mesh
Loci/STREAM, a pressure-based CFD solver, combined with a VoF module was used to conduct a series of simulations to verify the accuracy of the engineering model described in the previous section. The capabilities of the Loci/STREAM-VoF solver in standard gravity were first demonstrated by validation against the experimental results

of Goodridge [8]. The experimental setup used a 20 Hz sinusoidal forcing input from a shaker table to drive a 19.5 cm diameter circular cylinder with a fluid depth of 10 cm. Fluid properties for the simulation are provided in Table 1. Multiple views of the mesh are presented in Fig. 9. The mesh is constructed of approximately 19.4 million hexahedral cells, which provide the highest quality results using the VoF module. The nominal cell size in the high-resolution region around the interface is 0.5 mm. A semi-block structured meshing approach was used to build the tank interior with a nearly uniform volumetric cell size throughout.

The maximum time step was generally set to 1e-3 s – well below the 0.05 s pulse period – and further limited by the maximum Courant number (Co) of 0.2 in the computational domain. For the problems addressed in this study, a laminar flow regime was sufficient to capture the bulk movement of propellant in the tank and a first-order upwind advection scheme was used for robust convergence. Tank boundaries throughout this report were modeled as adiabatic walls, so no heat transfer into or out of the system was simulated. Acceleration inputs were applied to a non-inertial reference frame centered on the computational domain.

Table 1   Fluid property inputs for standard gravity validation cases.

| Fluid Property	Water	Air
Temperature (K)	345.15	
Static Pressure (bar)	1.01325	
Density (kg/m^3)	998.2	1.204
Dynamic Viscosity (Pa*s)	9.494e-4	1.825e-5
Surface Tension (N/m)	0.072	N/A
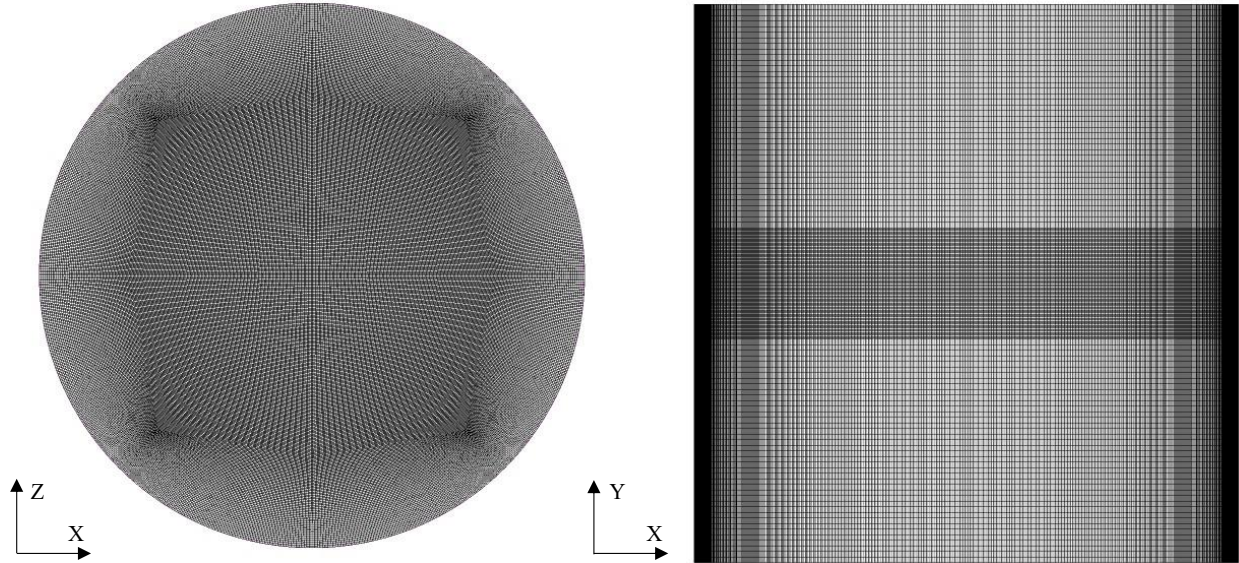
Fig. 9 Top view (looking down, left) and front view (right) of the mesh for the 19.5 cm diameter cylinder.

B. Droplet Ejection in Standard Gravity

The shaker table in the tests was ramped up in acceleration amplitude (a_{sine}) at the 20 Hz driving frequency until it excited Faraday waves (a_c), although the onset acceleration was not documented. Then, it was steadily increased until droplets were visibly broken off the surface. The ejection criteria defined by Goodridge et al. was two droplets observed within a 10 s period. This ejection thresholds (a_d) were recorded over a range of about 60 Hz for a variety of fluids and all the results subsequently collapsed into Eq. (15) and (16).

The pair of images in Fig. 10 illustrate the type of droplet-ejecting waves produced by the experiment and the CFD simulation. An excitation acceleration was not provided for the experimental photograph since it was only meant to be characteristic of liquid breakup in capillary waves. However, it compares well qualitatively to the CFD solution at twice the predicted ejection acceleration, which was calculated to be 6.8 m/s^2. The waves are highly irregular with

some long filaments, some short and blunt waves, and some droplets, particularly near the wall. The surface waves, and especially the droplets, become random in time and space at this unstable condition.
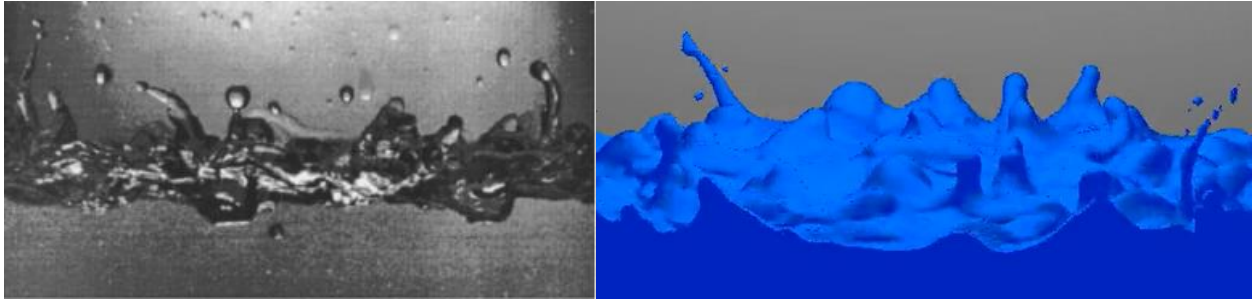
Fig. 10   **Droplet ejection using distilled water at 20 Hz. The experiment (left) shows droplets being ejected at an unspecified acceleration above the ejection threshold. The CFD simulation (right) excited at twice the ejection threshold also shows spikes forming and immediately breaking into droplets.**

The ejection criteria implies relatively infrequent breakup since the wave period is 0.05 s (1% of all wave periods liberate droplets). The authors estimated about 2-3% error in their threshold. The uncertainty on the prefactor introduced by Puthenveettil was about ± 20%, however. Therefore, the threshold is best understood as a band, as plotted on the design map. The CFD solution at the ejection threshold in Fig. 11 shows consistency with this banded threshold. The number of droplets is perhaps one every 1-2 s and a precise count likely depends strongly on mesh resolution. Most importantly, the simulations confirm that relatively infrequent droplets are forming at the acceleration that they are expected. Yang and Peugeot found similar conclusions with their validation of the CFD-ACE+ solver against these empirical results as well as other experiments carried out at the Marshall Space Flight Center [13].
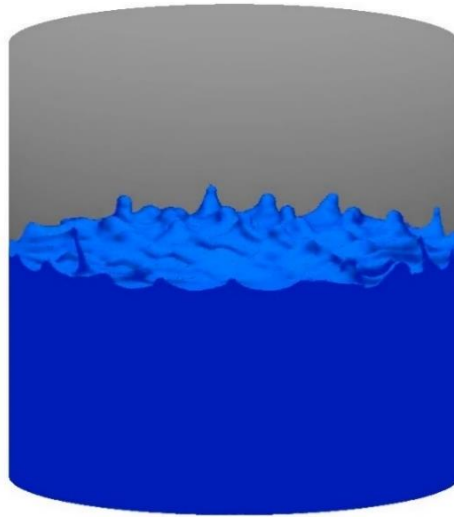
Fig. 11   **Droplets forming at the expected 20 Hz ejection threshold of 6.8 m/s^2.**

V. Verification of the Pulsed Settling Model in Microgravity

### A. Computational Domain and Mesh
A cryogenic propellant tank representative of a large-scale main tank for an orbital rocket was selected for these analyses. The total height from end to end is eight meters, the radius of the tank is two meters, the barrel section is four meters in height, and the forward and aft dome sections are two-meter radius hemispheres. An illustration of the tank, along with coordinate axes, is shown in Fig. 12. The origin of the coordinate system is at the center of the tank, but the coordinate axes are labeled outside of the tank for visibility. A single liquid fill level of 50% was chosen to typify an in-space environment, where a portion of the propellant has already been consumed. Separate analyses (not shown) with low fill levels (<10%) and high fill levels (>90%) are in accord with the conclusions presented here.

Two versions of the tank were meshed to demonstrate the impact of spatial dimensions (geometry) on the surface response. The primary three-dimensional tank used in the analyses is circular in cross-section comprising 11.1 million cells with a minimum cell size of about 0.0125 m. Hexahedral cells were used in a ± 0.5 m band around the interface and allowed to grow out as tetrahedral cells where no interface dynamics were anticipated. The two-dimensional rectangular tank in Fig. 13 was constructed with all hexahedral cells (74,580 cells) and a similar minimum cell size, but the cross section (into and out of the page) is a rectangle with a thickness of one cell.
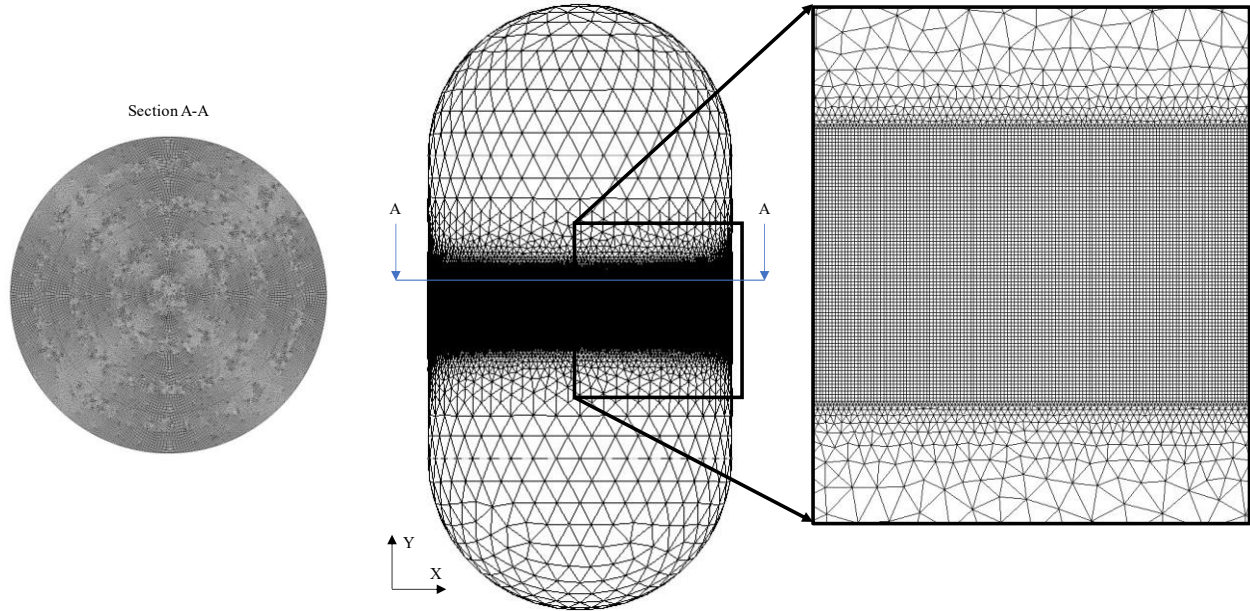
Fig. 12   Three-dimensional cylindrical propellant tank geometry and mesh.
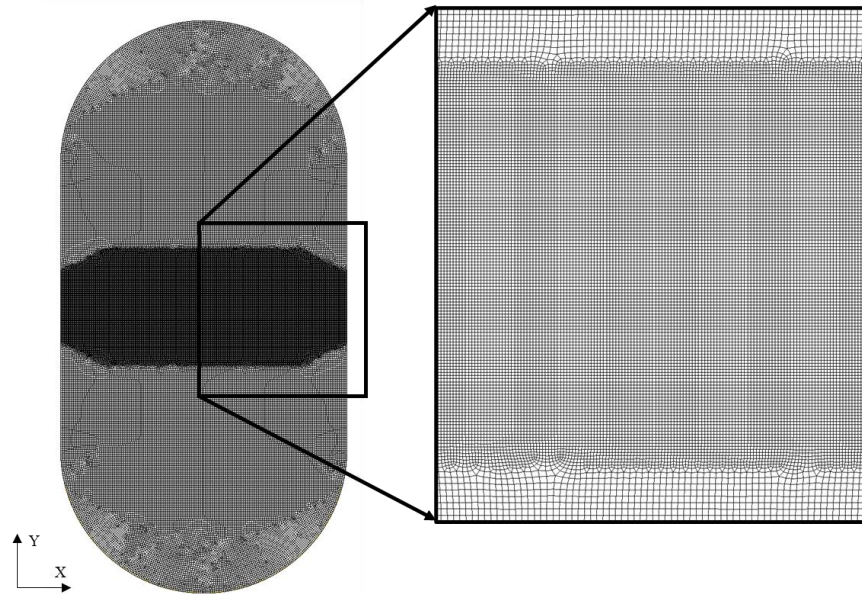
Fig. 13   Two-dimensional rectangular tank geometry and mesh. The thickness of the tank (into and out of the page) is one cell width.

B. Simulation Inputs

The liquid-vapor interface in all propellant tank simulations was initialized from a quiescent condition. The actual equilibrium condition will depend primarily on the axial acceleration at the start of the pulsed operation (if any), the

fluid properties, and the contact angle. Although there are some transient effects from the meniscus waves when starting from this simplified condition, the effects of Faraday waves are still apparent. Contact angles are typically very low for liquid cryogens, therefore a contact angle boundary condition of 10° was assumed in these cases. Since pulse widths were usually on the order of tenths of seconds, a timestep resolution of 0.01 s was used to ensure that pulses were fully resolved. A peak pulse acceleration of 0.1 m/s² was selected because it allowed for reasonable combinations of timesteps, pulse on-times, and duty cycles for CFD simulations.

Liquid oxygen (LOX) and gaseous oxygen (GOX) were chosen as the fluids due to their commonplace usage in modern rocketry. The engineering model should work equally well for other low-viscosity cryogens. Table 2 documents the fluid properties used for LOX and GOX in the propellant tank simulations. All propellant tank analyses were performed assuming liquid and vapor saturated at 1 bar. A future study devoted to the effects of heat transfer and mixing from Faraday waves could be undertaken with a hot ullage and a subcooled cryogen.

Table 2   Fluid property inputs CFD verification cases.

| Fluid Property	LOX	GOX
Temperature (K)	90.0621	
Static Pressure (bar)	1	
Density (kg/m³)	1141.796	4.413
Dynamic Viscosity (Pa*s)	1.953e-4	6.94e-6
Surface Tension (N/m)	0.013177	N/A

In the next few sections, the propellant tank geometry was analyzed at various points on the design map. Simulations discussed or shown in sections C and D are plotted in Fig. 14, though this is not an exhaustive list of evaluated cases. These operating conditions were selected to represent the behavior over a broad range of duty cycles, around the droplet ejection threshold, and within the Faraday response region. Contour lines of ½-subharmonic mode numbers for the cylindrical propellant tank intersect each point to give an impression of how the response varies as frequency and acceleration change. For ease of visualization, the azimuthal mode number (n) is fixed at 0 and radial mode numbers (m) are shown. As discussed later, three-dimensional tanks have competing modes as frequency increases. The contour lines shift to the right for higher azimuthal mode numbers and may overlap other (n, m) pairs.
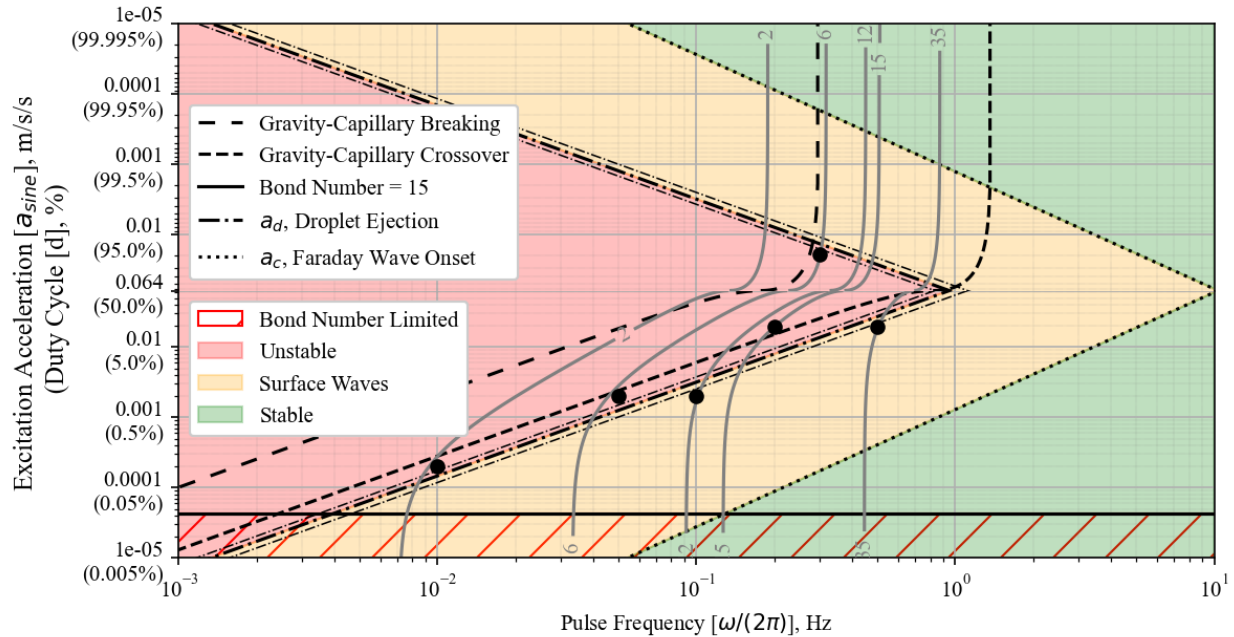
Fig. 14   Design map with contours of cylindrical tank radial mode numbers (solid grey, n held at 0) and selected points analyzed in subsequent sections overlaid.

C. Droplet Ejection in Microgravity

After establishing the reliability of the CFD solver to predict liquid breakup in standard gravity, the engineering model was extended to a microgravity environment. In this context, the sole contributor to acceleration is the pulsed settling. No data was immediately available to validate the model and CFD results in reduced gravity. One potentially germane experiment, however, is the Gator GATSBY ("GrAvitational effecTS on the faraday instaBilitY'). The International Space Station (ISS) project was organized by the University of Florida and videos were generously shared while analysis of the results is currently underway [14]. The team excited two liquids, FC72 and Silicone Oil, in an 8 mm by 32 mm by 20 mm box with a sinusoidal forcing input orthogonal to the interface of the two fluids. Images in Fig. 15 confirm that subharmonic Faraday waves were generated in microgravity at a driving frequency of 2.5 Hz. Vibrations were even increased significantly enough to break the interface (not shown). Observation of waves provides some qualitative reinforcement of the engineering model with the possibility of future validation.


a)   b)
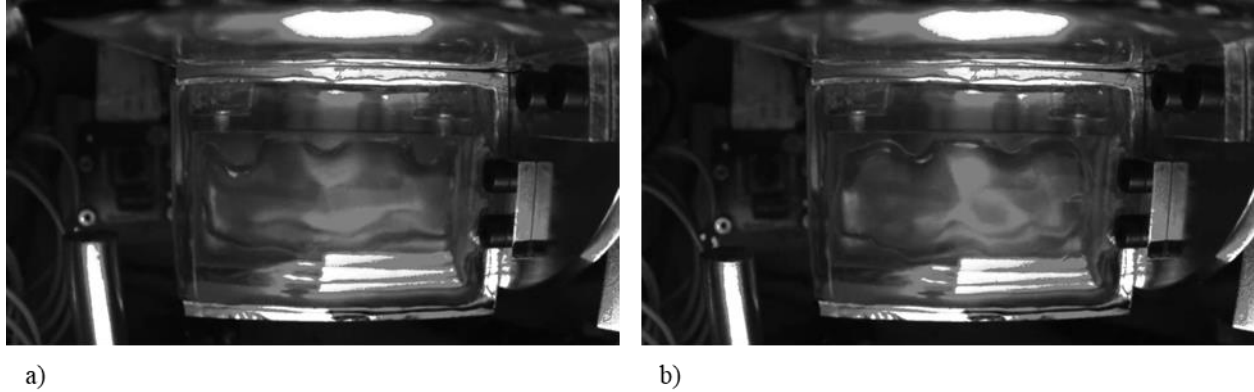
Fig. 15   Subharmonic Faraday waves in microgravity captured by the ISS project, Gator GATSBY. Images a) and b) show the change in interface shape over 0.4 s, or one forcing period (half of one wave period) [14].

Examples of interface deformation in the unstable region are shown in Fig. 16 and Fig. 17. The pulse frequencies are 0.2 Hz and 0.05 Hz and duty cycles are 10% and 1%, respectively. The engineering model accurately predicts that these operating conditions result in droplet ejection. Comparable to the validation in standard gravity, the pulsed forcing profile raises ligaments well above the surface where they then separate and break up. Wave motions are chaotic in these conditions. Still, the impact of frequency is apparent in the wavelengths when looking at the top-down views. The 0.2 Hz, 10% duty cycle result has much thinner ligaments than the 0.05 Hz, 1% duty cycle condition.
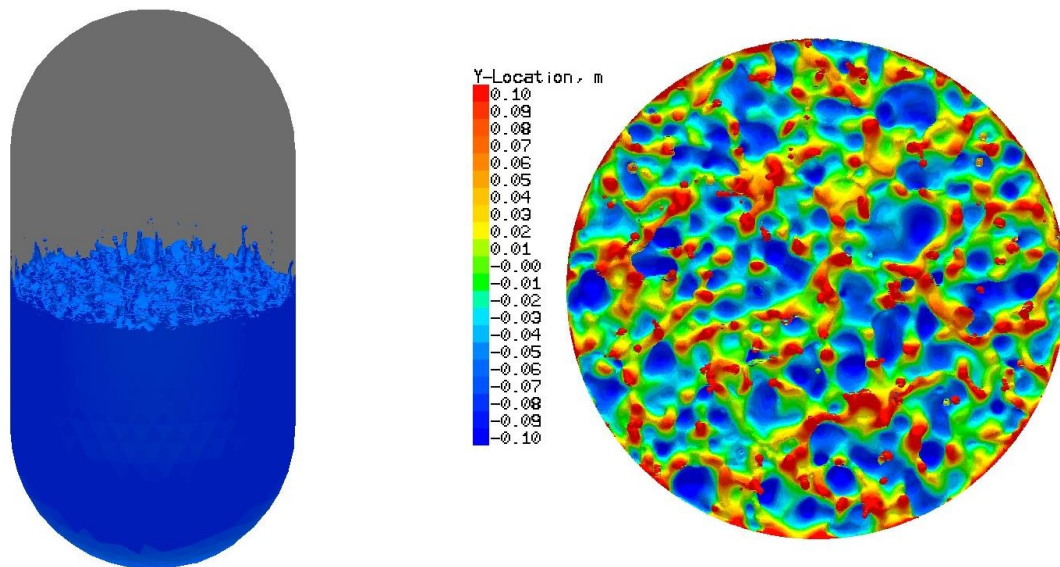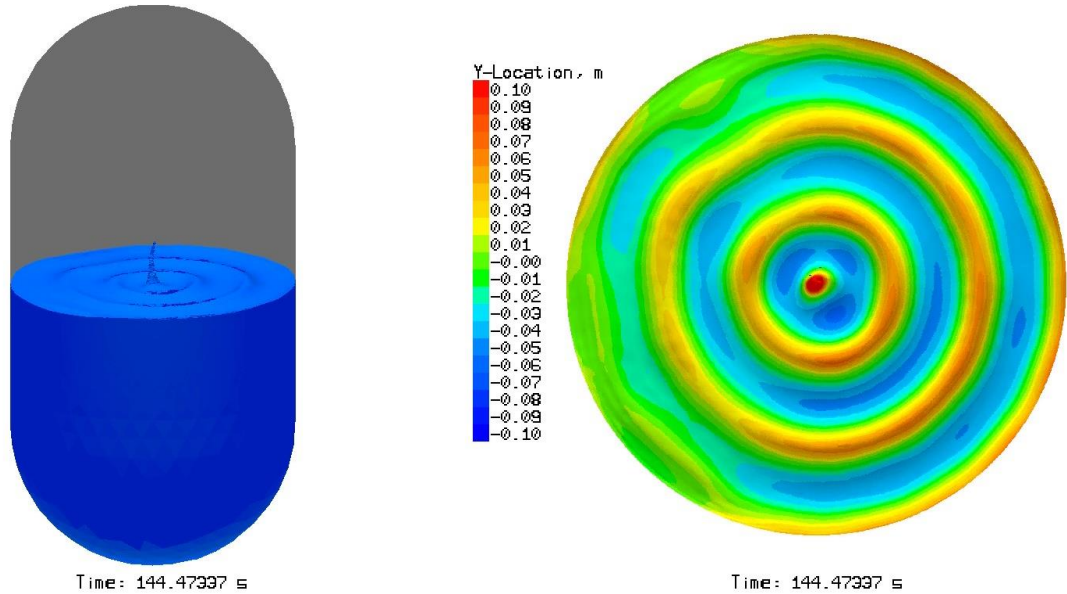

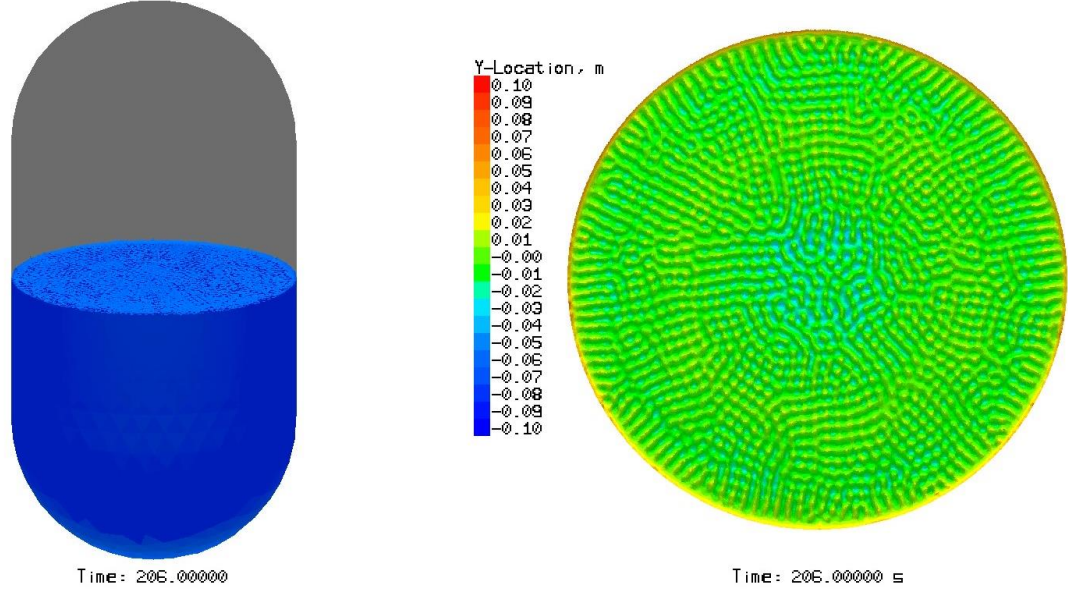**Fig. 16   Droplet ejection at 10% duty cycle with a pulse on-time of 0.5 s (0.2 Hz).**

14
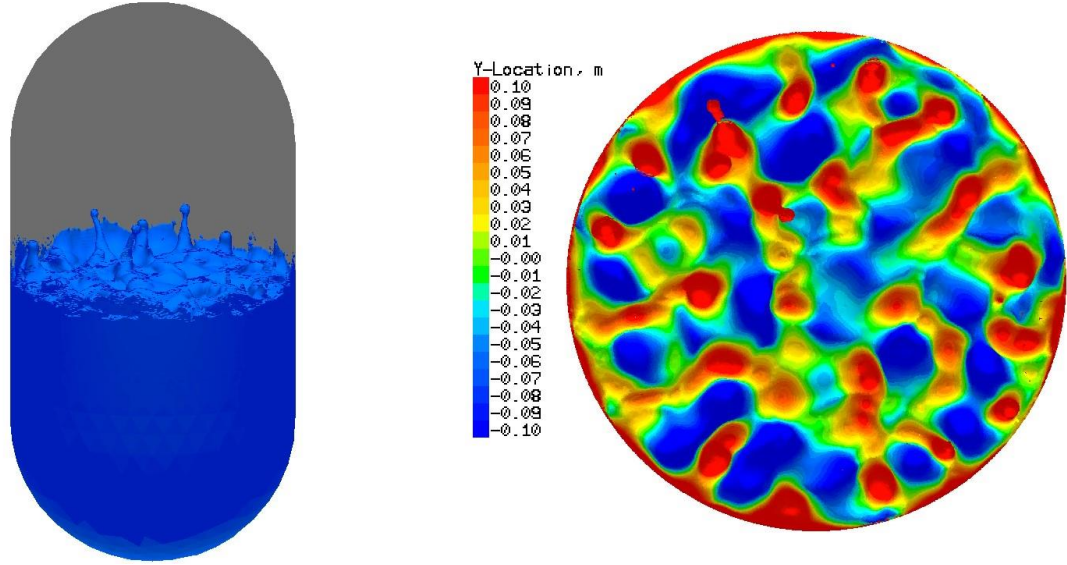
Fig. 17   Droplet ejection at 1% duty cycle with a pulse on-time of 0.2 s (0.05 Hz).

The droplet ejection threshold equation is built on assumptions that the point of interest is far to the right of the capillary-gravity breaking line ($\omega^* \gg 0.61$), so it is expected to become less reliable for the 90% duty cycle, 0.3 Hz case. Indeed, although some local breakup is observed in Fig. 18 due to constructive interference between modes, the overall interface is not as prone to breakup globally.

Fig. 18   Local droplet ejection at the center of the tank at 90% duty cycle and a pulse width of 3 s (0.3 Hz).

As for the points in the yellow region of Fig. 14, the model correctly identified these as high amplitude (for the applied duty cycle), but without forming droplets. Both cases at 1% and 10% duty cycles failed to break the interface, but instead, continued steadily with hemispherical caps oscillating in subharmonic motion. A snapshot of the 10% duty cycle, 0.5 Hz pulse frequency result is illustrated in Fig. 19. Notably, the difference in driving frequency between the low, steady oscillation at this duty cycle and the substantial droplet-ejecting state in Fig. 16 is only 0.3 Hz. This underscores the importance of ensuring that hardware tolerances and design margins will position the system in a stable configuration.

15

Fig. 19   Surface wave heights below droplet ejection at 10% duty cycle and a pulse width of 0.2 s (0.5 Hz).

D. Surface Modal Responses

Surface waves produced by pulsed settling were evaluated for consistency with analytical equations. For a circular cylinder, the wavenumber can be calculated with Eq. (13) while Eq. (12) can be used for a rectangular tank. Since the wave frequency of the ½-subharmonic is half the pulse frequency, Eq. (8) is combined with the wavenumber equation appropriate for the tank to estimate the mode shape. Two-dimensional rectangular tanks only have a single node count. Cylindrical mode shapes, on the other hand, are expressed as (n, m) pairs indicating the number of nodal diameters and circles, respectively. Imaging of the first 50 modes in a cylindrical tank were documented by Shao, et al. [15].

Surface shapes may take various forms over time, exemplified by the sequence in Fig. 20. At the pulsing inception, harmonic edge waves are propagated towards the center according to a $(0, 21)$ or $(0, 22)$ pattern for a driving frequency of 0.3 Hz at 90% duty cycle. However, these waves yield to the dominant ½-subharmonic waves in part b) of the image. A $(0, 6)$ mode takes over as the most visible response, although a distinct high-order circumferential mode is also observed at the same time. As the simulation continues to evolve in part c), mode mixing begins to distort and warp the shapes into a mosaic of interfering patterns.


a)   b)   c)
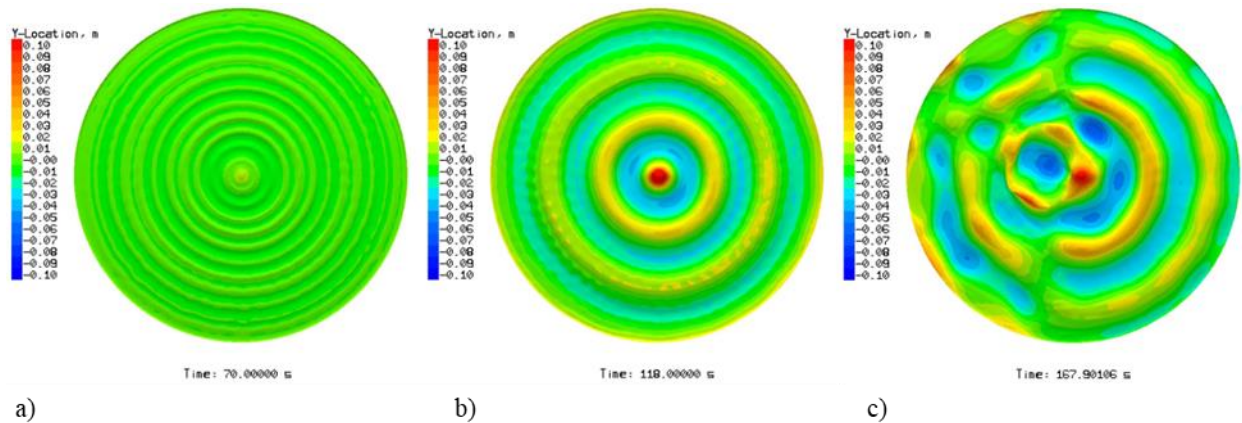
Fig. 20   Transient CFD mode shapes for a cylindrical tank at 90% duty cycle and 3 s pulse on-time (0.3 Hz). Image a) shows the initial harmonic waves, b) displays the higher amplitude subharmonic waves which take over, and c) shows how additional high-order modes begin to mix and interfere.

An excellent example of predicting the surface response through CFD is the $(0, 2)$ mode shown in the top-down view in Fig. 21. As one of the lowest modes, there is little interference from other wave shapes. There is also

consistency between both cylindrical and rectangular tanks with respect to the interface shape. The calculated natural frequency of this response is 0.00464 Hz, which is almost exactly half of the pulse frequency, as expected. As the frequency increases for a given duty cycle though, competition between modes and mixing becomes more probable. The surface of the cylindrical tank in Fig. 22 appears to be vibrating in a (8, 4) arrangement. The associated natural frequency of (8, 4) is 0.0249 Hz – once again, corresponding to half of the pulse frequency. A different nodal count – about $m = 7$ – is shown in the rectangular tank. The natural frequency of the $m = 7$ rectangular tank mode (0.0258 Hz) is nearly equivalent to that of the (8, 4) cylindrical response. In fact, even for the cylindrical tank alone there are several (n, m) pairs that would produce a similar value to (8, 4): (1, 7), (3, 6), (6, 5), (11, 3), and more.
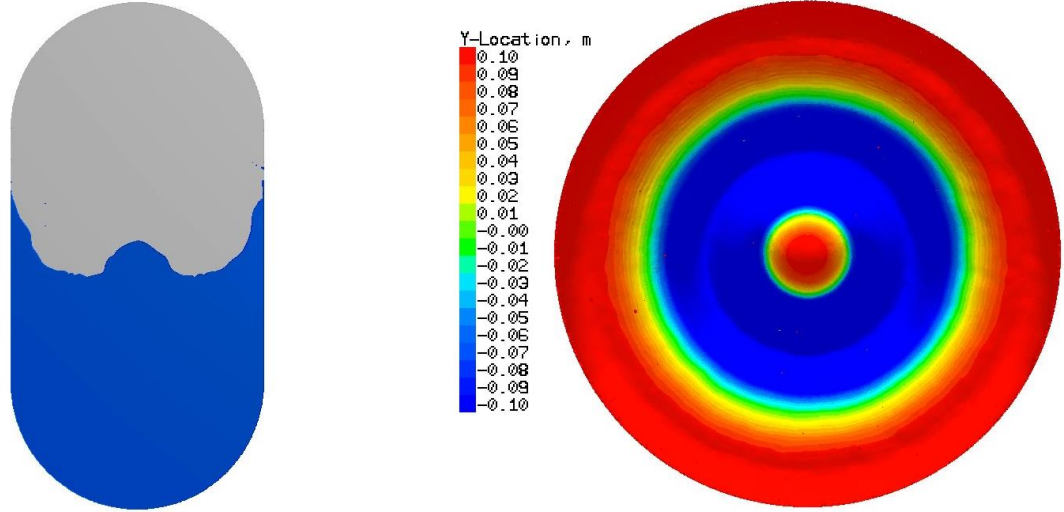
Fig. 21   CFD mode shape for a two-dimensional rectangular tank (left) and cylindrical tank (right) at 0.1% duty cycle and 0.1 s pulse width (0.01 Hz).
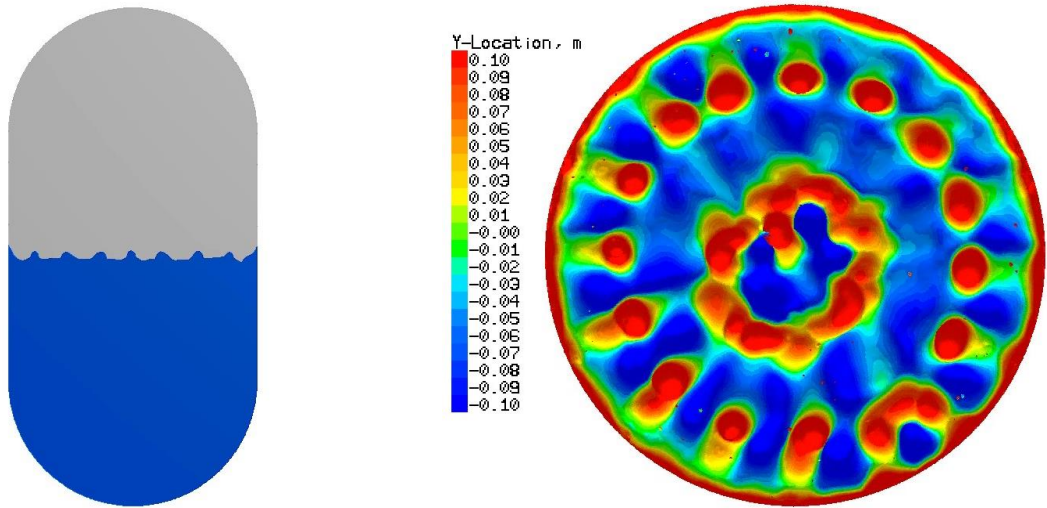

Fig. 22   CFD mode shape for a two-dimensional rectangular tank (left) and cylindrical tank (right) at 1% duty cycle and 0.2 s pulse width (0.05 Hz).

E. Wave Amplitude Predictions

The estimation of wave amplitude may be valuable in a cryogenic tank for heat transfer modeling. The impact of lateral slosh wave amplitude on pressure and temperature were explored by Ludwig, Dreyer, and Hopfinger [16] via a sloshing Reynolds number and Nusselt number. Although it is not the same manner of motion, Faraday waves and their disruption of the thermal stratification around the interface could potentially be modeled in kind.

Experiments have documented linear behavior between the wave amplitude of non-breaking waves and the amplitude of the sinusoidal displacement function. For the sinusoidal acceleration in Eq. (20), the double integral is the sinusoidal displacement (a_{sine}/ω^2). Goodridge observed that capillary waves respond linearly according to Eq. (14). Using this relationship for wave amplitude entails that the ratio of wave amplitude to wavelength (rearrange Eq. (8) and Eq. (11)) is unity at the droplet ejection threshold, consistent with their initial assumptions. Jiang, Perlin, and Schultz also documented a linear movement of wave amplitude with the sinusoidal displacement amplitude, albeit at a much lower rate [17]. Once droplet ejection began, they measured wave amplitudes at substantially higher values.
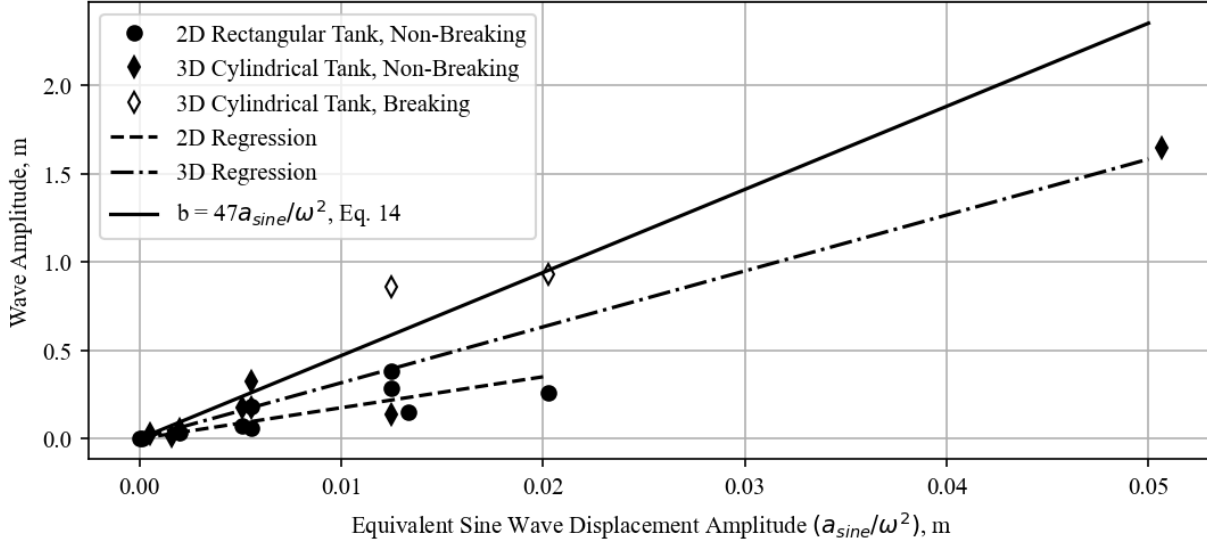
Fig. 23   Average wave amplitude vs. a_{sine}/ω^2 for many two-dimensional rectangular tank cases.

Wave amplitudes in the propellant tank were measured by the maximum and minimum values of the VoF = 0.5 (cells with 50% liquid in them) iso-surface within the inner 80% radius of the tank. Using a clipped radius removes the meniscus from the calculation, which can extend much higher than the waves oscillate. The range is then divided in half to obtain the amplitude of the surface waves. As Fig. 7 showed, the wave amplitudes can vary with time, so an average of the last twenty peak amplitudes was taken. A composite of the 3D cylindrical tank and 2D rectangular tank cases is given in Fig. 23. Regression lines are overlaid with the y-intercept forced through the (0, 0) point. The data points suggest that Eq. (14) is a conservatively high estimate, with lower slopes of 31.6 and 17.5 for the cylindrical tank and rectangular tank, respectively. However, if some of the operating conditions with ejected droplets are included, a slope of 47 appears to better capture the height of those surface elevations. It is not clear whether Goodridge et al. were referring to breaking or non-breaking capillary waves when their observations confirmed a slope of 47.

VI. Conclusion

An engineering model for assessing the stability of a liquid surface in microgravity which is subject to pulsed accelerations perpendicular to the interface was compiled and verified with CFD. Validation of the CFD solver against experimental data in standard gravity provided confidence in the tool's ability to forecast surface behavior in conditions where experimental data is sparse. The engineering model relies on empirical and theoretical formulae developed for sinusoidal forcing. Consequently, a method for converting the pulsed forcing waveform into an equivalent sinusoidal wave amplitude was proposed. Several methods were considered, included conserving the average power of the wave, but the recommended method of using the first harmonic resulted in good agreement.

Predictions made using the pulsed settling engineering model are in good agreement with CFD solutions showing droplet breakup and surface wave characteristics such as the subharmonic frequency response and mode shape. Wave amplitude is more complex to determine accurately, but scaled functions can serve as rules of thumb if estimates are needed. The Faraday wave onset criterion was not scrutinized closely like other characteristics presented here. Computationally, very small cell sizes are required to resolve the waves at those frequencies and acceleration levels, requiring larger meshes and time. Practically, the risk of ullage collapse should be very low around this boundary, so the threshold should largely serve as a helpful target for designers who are deciding how much margin to build into their systems.

Acknowledgments

References

[1] Faraday, M., "On the Forms and States assumed by Fluids in contact with vibrating elastic surfaces," an appendix to "On a peculiar class of Acoustical Figures," Philosophical Transactions of the Royal Society, Vol. 121, 1831 (Parts I and II), pp. 299-340.

[2] Douady, S., "Experimental study of the Faraday instability," Journal of Fluid Mechanics, Vol. 221, 1990, pp. 383-409. doi:10.1017/S0022112090003603

[3] Hochstein, J.I., and Chato, D.J., "Pulsed Thrust Propellant Reorientation: Concept and Modeling," Journal of Propulsion and Power, Vol. 8, No. 4, 1992, pp. 770-777.

[4] Edwards, W.S. and Fauve, S., "Patterns and quasi-patterns in the Faraday experiment," Journal of Fluid Mechanics, Vol. 278, 1994, pp. 123-148.

[5] Benjamin, T.B. and Ursell, F., "The Stability of the Plane Free Surface of a Liquid in Vertical Periodic Motion," Proceedings of the Royal Society of London. Series A, Mathematical and Physical Sciences, Vol. 225, 1954, pp. 505-515.

[6] Kumar, K. and Tuckerman, L.S., "Parametric instability of the interface between two fluids," Journal of Fluid Mechanics, Vol. 279, 1994, pp. 49-68.

[7] Kundu, P.K., Cohen, I.M., and Dowling, D.R., *Fluid Mechanics*, 5th ed., Academic Press, Waltham, MA, 2012, Ch. 7.

[8] Goodridge, C.L., Tao Shi, W., Henschel, H.G.E., and Lathrop, D.P., "Viscous effects in droplet-ejecting capillary waves," Physical Review E, Vol. 56, No.1, 1997, pp. 472-475.

[9] Goodridge, C.L., Tao Shi, W., and Lathrop, D.P., "Threshold Dynamics of Singular Gravity-Capillary Waves," Physical Review Letters, Vol. 76, No.11, 1996, pp. 1824-1827.

[10] Crapper, G.D., "An Exact Solution for Progressive Capillary Waves of Arbitrary Amplitude," Journal of Fluid Mechanics, Vol. 2, No. 6, 1957, pp. 532-540.

[11] Puthenveettil, B.A. and Hopfinger, E.J., "Evolution and breaking of parametrically forced capillary waves in a circular cylinder," Journal of Fluid Mechanics, Vol. 633, 2009, pp. 355-379. doi:10.1017/S0022112009007162.

[12] Hoffman, B.D. and Brodnick, J.M., "Operational Techniques in Microgravity for Cryogenic Fluid Management," AIAA 2023-1217. AIAA SciTech 2023 Forum. January, 2023. doi:10.2514/6.2023-1217.

[13] Yang, H.Q. and Peugeot, J., "Surface Instability of Liquid Propellants under Vertical Oscillatory Forcing," AIAA 2011-5773. 47th AIAA/ASME/SAE/ASEE Joint Propulsion Center and Exhibit. July, 2011. doi:10.2514/6.2011-5773.

[14] From ISS: Gravitational Effects on the Faraday Instability- NSF 2025117- PI. R. Narayanan- team: J. Livesay, R. Singiser, Z. Karpinski and R. Narayanan.

[15] Shao, X., et al., "Surface Wave Pattern Formation in a Cylindrical Container," Journal of Fluid Mechanics, Vol. 915, 2021, pp. A19-1 – A19-19. doi:10.1017/jfm.2021.97.

[16] Ludwig, C., Dreyer, M. E., and Hopfinger, E.J., "Pressure Variations in a Cryogenic Liquid Storage Tank Subjected to Periodic Excitations," International Journal of Heat and Mass Transfer, Vol. 66, 2013, pp. 223-234.

[17] Jiang, L., Perlin, M., and Shultz, W., "Steep and Breaking Faraday Waves," National Research Council. 1997. Twenty-First Symposium on Naval Hydrodynamics, pp. 812-826. Washington, DC: The National Academies Press. doi:10.17226/5870.